

## WIDEBAND VLA OBSERVATIONS OF ABELL 2256 I: CONTINUUM, ROTATION MEASURE AND SPECTRAL IMAGING

FRAZER N. OWEN,<sup>1</sup> LAWRENCE RUDNICK,<sup>2</sup> JEAN EILEK,<sup>3,4</sup> URVASHI RAU,<sup>1</sup> SANJAY BHATNAGAR,<sup>1</sup> LEONID KOGAN,<sup>1</sup>  
*ApJ in press; Received April 3, 2014; Accepted: August 19, 2014*

### ABSTRACT

We report new observations of Abell 2256 with the Karl G. Jansky Very Large Array (VLA) at frequencies between 1 and 8 GHz. These observations take advantage of the 2:1 bandwidths available during a single observation to study the spectral index, polarization and Rotation Measure as well as using the associated higher sensitivity per unit time to image total intensity features down to  $\sim 0.5''$  resolution. We find the Large Relic, which dominates the cluster, is made up of a complex of filaments which show correlated distributions in intensity, spectral index, and fractional polarization. The Rotation Measure varies across the face of the Large Relic but is not well correlated with the other properties of the source. The shape of individual filaments suggests that the Large Relic is at least 25 kpc thick. We detect a low surface brightness arc connecting the Large Relic to the Halo and other radio structures suggesting a physical connection between these features. The center of the F-complex is dominated by a very steep-spectrum, polarized, ring-like structure, F2, without an obvious optical identification, but the entire F-complex does have interesting morphological similarities to the radio structure of NGC1265. Source C, the Long Tail, is unresolved in width near the galaxy core and is  $\lesssim 100$  pc in diameter there. This morphology suggests either that C is a one-sided jet or that the bending of the tails takes place very near the core, consistent with the parent galaxy having undergone extreme stripping. Overall it seems that many of the unusual phenomena can be understood in the context of Abell 2256 being near the pericenter of a slightly off-axis merger between a cluster and a smaller group. Given the lack of evidence for a strong shock associated with the Large Relic, other models should be considered, such as reconnection between two large-scale magnetic domains.

*Subject headings:* galaxies: observations — galaxies: clusters: individual (Abell 2256) — galaxies: clusters: intracluster medium — galaxies: jets— galaxies: magnetic fields—radio continuum: galaxies

### 1. INTRODUCTION

Abell 2256 contains perhaps the richest variety of radio phenomena of any known rich cluster (e.g., Bridle & Fomalont 1976; Bridle et al. 1979; Röttgering et al. 1994; Clarke & Ensslin 2006; Kale & Dwarakanath 2010; van Weeren et al. 2012a). The Mpc-scale, relatively flat spectrum, diffuse structure – often called a radio relic – is perhaps the most intriguing (e.g., Clarke & Ensslin 2006). It shows many similarities to the general class of radio relics, which are the large, often elongated structures found near the periphery of many clusters (e.g., Feretti et al. 2012). Because of their location and the lack of any association with a cluster galaxy, such relics are generally thought to be caused by large-scale shocks generated in cluster mergers (e.g., Brunetti & Jones 2014).

There is also a radio halo roughly coincident with the X-ray emission (e.g., Clarke & Ensslin 2006), several radio tails including one which is extremely straight over its  $\gtrsim 500$  kpc length (e.g., Röttgering et al. 1994; Miller, Owen & Hill 2003; Brentjens 2008), a complex of very steep spectrum emission (the F-complex) most of which is not clearly associated with any cluster member (e.g.,

Röttgering et al. 1994; Miller, Owen & Hill 2003) and more than 40 cluster members with detected radio emission (Miller, Owen & Hill 2003).

Abell 2256 ( $z = 0.0583$ ) is an Abell richness class 2, massive cluster, with an estimated total mass of  $\sim 10^{15} M_{\odot}$  within 1 Mpc of the cluster center (Berrington, Lugger & Cohn 2002; Mohr et al. 1999). The cluster has been proposed to be an ongoing merger (Fabricant, Kent & Kurtz 1989; Fabian & Daines 1991) of two or three previously independent clusters (Berrington, Lugger & Cohn 2002). The cluster appears to be in the early or mid-stages of its merger (Roettiger, Burns & Pinkney 1995; Sun et al. 2002) and thus may allow us to study some of the environmental changes resulting from such mergers while they are taking place.

The EVLA project, which has increased the frequency coverage, bandwidth and number of channels that can be observed in a single observation with VLA, gives us an important new tool to study these phenomena. Here we report initial observations using these capabilities to study the total intensity and polarization of the emission from Abell 2256 in the 1-8 GHz range. This paper is the first in a series analyzing the results of these new observations. This paper is intended to introduce and summarize the new results we have obtained. Later papers are planned which will address in more detail 1) the cluster magnetic field based on the Faraday Rotation of individual sources, 2) the physics of the individual radio galaxies in Abell 2256, 3) the physics of the Large Relic, and 4) the radio properties of the cluster galaxy

<sup>1</sup> National Radio Astronomy Observatory, P. O. Box O, Socorro, NM 87801 USA.; fowen@nrao.edu. The National Radio Astronomy Observatory is facility of the National Science Foundation operated under cooperative agreement by Associated Universities Inc.

<sup>2</sup> University of Minnesota

<sup>3</sup> Adjunct Astronomer at the National Radio Astronomy Observatory

<sup>4</sup> New Mexico Tech

TABLE 1  
SUMMARY OF OBSERVATIONS

Config	Date	GHz	Hours
D	29-JUL-2010	1 – 2	3
C	31-OCT-2010	1 – 2	6
B	21-MAR-2011	1 – 2	5
B	10-APR-2011	1 – 2	6
A	26-OCT-2012	1 – 2	3
A	28-OCT-2012	1 – 2	3
A	30-OCT-2012	1 – 2	3
A	17-OCT-2012	2 – 4	3
A	23-OCT-2012	2 – 4	3
A	12-OCT-2012	4 – 6	3
A	24-OCT-2012	4 – 6	3
A	25-OCT-2012	4 – 6	3
A	09-OCT-2012	6 – 8	3

population.

This paper is divided into 5 sections. In §2 we cover observations, editing, calibration and imaging of the VLA wideband data. In section §3, we present the basic results from the project. In section §4 we discuss the broader implications for understanding Abell 2256 and in §5 we summarize our most important conclusions. We will assume  $H_0=70 \text{ km s}^{-1} \text{ Mpc}^{-1}$ ,  $\Omega_M = 0.27$ ,  $\Omega_{vac} = 0.73$  in what follows.

## 2. OBSERVATIONS, EDITING, CALIBRATION & IMAGING

Data were obtained in the A, B, C and D configurations as summarized in Table 1. The 8 or 16 subbands of 128 MHz each were used to cover the frequency range from 1-2, 2-4, 4-6, and 6-8 GHz. Each subband had 64 2MHz channels. About one third of the full bandwidth was lost due to interference in the 1-2 GHz range, especially in the range 1500-1648 MHz. Much less, but significant interference was encountered in the other bands. At each band observations were made in 4 to 8 hour scheduling blocks with the Abell 2256 field observed in scans of 20 – 25 minutes each bracketed by a phase calibrator, either J1634+6245 or J1800+7828. 3C48 was used as the flux density calibrator and 3C138 was used as the polarization position angle calibrator.

The calibration was carried out in the standard way using AIPS, except for a few changes needed to deal with the very wide bandwidth. The bandpass was calculated using the phase calibrator, only without any calibration except for the delay correction. These data were then self-calibrated in phase only and then a single bandpass solution for each observed track was derived using BPASS. This procedure has the effect of averaging out most of the interference since the interfering signals are mostly either from satellites or from sources on the ground and thus their observed phases change rapidly with respect to sources in the sky.

Using the delay and bandpass corrections only, the data were then flagged using the AIPS task RFLAG. This task uses the fact that the phase of the interference changes rapidly with respect to the astronomical sources, as well as the fact that the interference typically is not circularly polarized and thus shows up much more prominently in the cross-hand correlations used to observe linear polarization. RFLAG was used to calculate the vector rms of groups of three adjacent integrations (in time) on each baseline in each channel in each subband

for the RL and LR correlations. Then all the correlations were flagged for the middle of the three integrations when the rms was found to be about  $5\sigma$  above the mean rms for that subband and baseline. For more details see Greisen (2014). Flagging was also done for the first two and last two channels for each subband and a few other channels that were spoiled by the correlator. The 1500-1648 and 2128-2384 MHz frequency ranges were also entirely removed. This procedure cleans up enough of the interference so that it is not a serious problem for the rest of the calibration and imaging.

However the sensitivity does still vary across the full band and with respect to time due to the instrument itself and to the residual interference. After amplitude and phase calibration, the task REWAY was used to calibrate the weights by calculating the rms as a function of time for each baseline and subband across the unflagged channels. In this way an empirical weight could be assigned to each visibility in calibrated units of  $\text{Jy}^{-2}$ .

The ionospheric Rotation Measure (RM) was corrected using the AIPS procedure VLATECR which uses a time variable atmospheric model of the ionosphere and the earth's magnetic field. In practice these corrections were negligible during all the times of these observations. The polarization calibration was done in the standard way in AIPS (Greisen 2014) except that the calibration for instrumental polarization and position angle were done as a function of channel. A narrowband image of the Abell 2256 field near the center of each band was made in AIPS using the task IMAGR. These images were used to self-calibrate the phases for each band before applying the polarization corrections. For each subband the position angle calibration was generally accurate to better than 1 degree and the instrumental polarization was corrected to better than a few tenths of a percent.

The total intensity imaging was carried out in CASA using the MSMFS deconvolution algorithm (Rau & Cornwell 2011). This algorithm, as implemented in the CASA task `clean`, deconvolves the image using multiple scales and multiple Taylor coefficients as a function of frequency to describe the spatial intensity distribution over the full observed bandwidth. CASA `clean` uses the W-projection which corrects for the sky curvature, so that we could make one large image which covered the entire field. The output products of interest are a total intensity image at a reference frequency and a spectral index image. After imaging with CASA `clean`, the CASA task `widebandpbc` was used to correct all the output images for the primary beam attenuation.

In addition we provide spectral index error images. The errors in the spectral index image are a combination of random errors in the calibrated visibilities and imperfections in the deconvolution process. In order to include both error sources, the spectral index error map is derived by propagating residual errors in the individual Taylor coefficient maps through the division that calculates the spectral index value. To account for per pixel residuals as well as global noise levels, an error estimate was computed as

$$\Delta I_\alpha = \sqrt{(\Delta I_\alpha^{global})^2 + (g \Delta I_\alpha^{pixel})^2} \quad (1)$$

where  $\Delta I_\alpha^{global}$  and  $\Delta I_\alpha^{pixel}$  are calculated according to

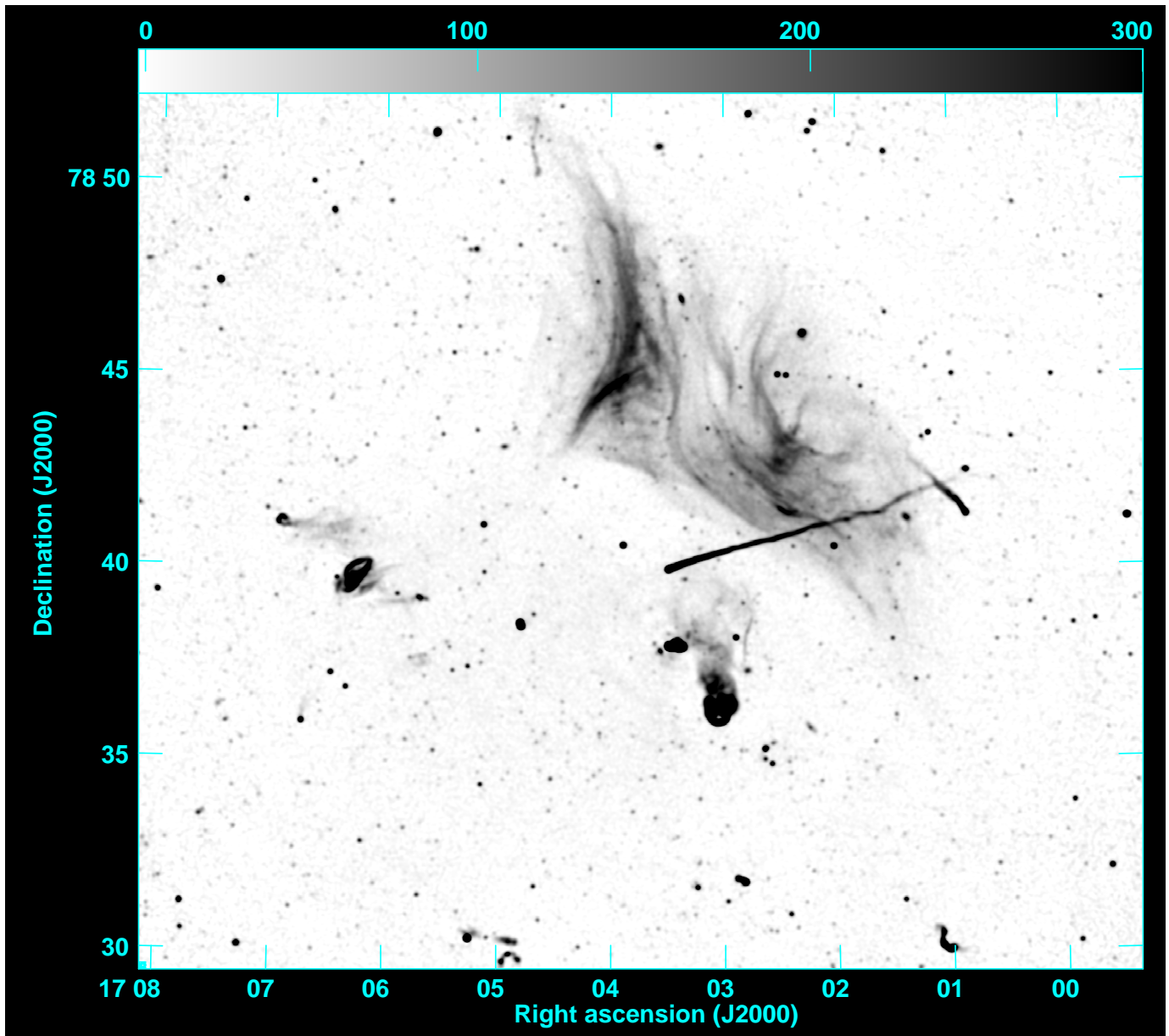


FIG. 1.— Grey-scale radio image of A2256 at  $6''$  (clean beam) resolution. The intensity wedge at the top of the figure shows the brightness in  $\mu\text{Jy/beam}$ .

equation 39 of Rau & Cornwell (2011), with the global error per Taylor coefficient computed as the median of the absolute deviation from the median of all pixel amplitudes in the residual image, and the per-pixel error read off directly from the Taylor coefficient residual images. We determined the value of  $g$  from the small-scale spectral index scatter in the  $6''$  resolution spectral index image. We find the best value for  $g$  is 0.03. In this way we have generated a spectral index error estimate at each point in the image. The same value for  $g$ , 0.03, is used for the  $12''$  image which we find is consistent with the scatter in  $\alpha$  on that image.

The polarization imaging was done in AIPS. We first calculated cubes of Q and U using 10 MHz channels. The spectral range below 1250 MHz was not useful due to the final polarizers not being available for L-band (1-2 GHz). The AIPS task IMAGR was used with multi-scales and faceting appropriate to correct for the sky curvature. The

facets were assembled into two monolithic cubes using FLATN which cover the entire field.

The output cubes were corrected for spectral index and primary beam attenuation with the task SPCOR, using the spectral index image from CASA. Then the task FARS was used to calculate a RM-synthesis cube (Brentjens & de Bruyn 2005) from which we can derive, among other things the maximum polarized flux and the corresponding Rotation Measure for each pixel. These techniques will be discussed more in a later paper.

The total intensity, polarization and RM-synthesis images are each calculated at a number of resolutions to emphasize different features in the data. Each image was made using all of the unflagged data. Various combinations of Briggs robust weighting in CASA and a uv-taper were used to modify the output synthesized beam. A range of modeling scales, ranging from 0 to the maximum minor axis size of a feature bright enough to be detected,

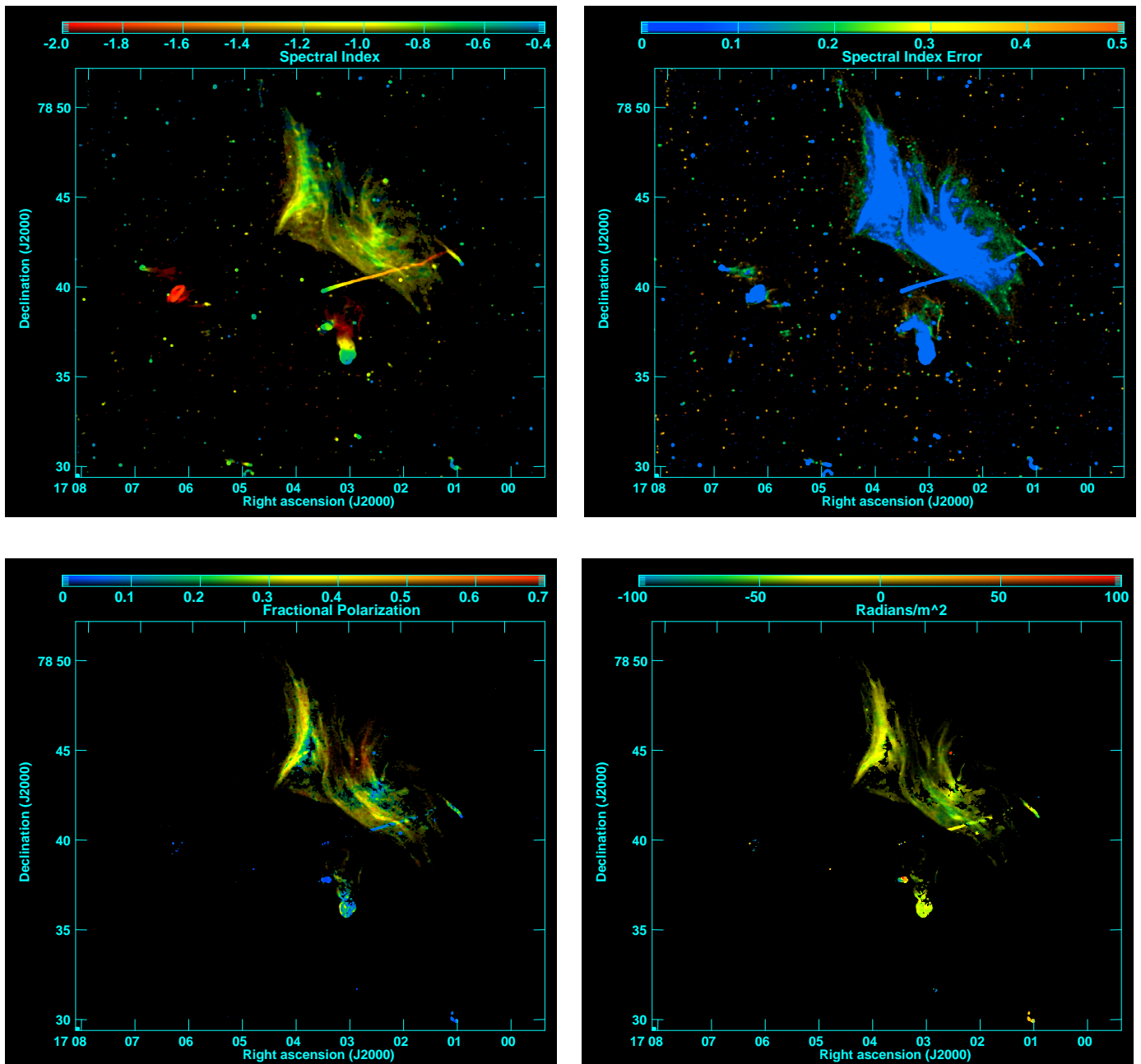


FIG. 2.— Wide-field images of the Abell 2256 field. Top left, “true” color radio image of A2256. The intensity image has a  $6''$  circular clean beam and the color has a  $12''$  circular clean beam. The color bar shows spectral index  $\alpha$  from -2.0 to -0.4,  $S \propto \nu^\alpha$ . Top right, spectral index error image of A2256 quantized in steps,  $0 - 0.1$ ,  $0.1 - 0.2$ ,  $0.2 - 0.3$ ,  $0.3 - 0.4$  and  $0.4 - 0.5$  with the same clean beam sizes as the top left panel. Lower left, Fractional Polarization at  $6''$  resolution. The color bar shows the fractional polarization levels from 0 to 0.70. Lower right, RM Max from AFARS at  $6''$  resolution. The color bar shows RM values between  $-100$  and  $+100$   $\text{rad/m}^2$ . RM values beyond the  $-100$  to  $100$   $\text{rad/m}^2$  range are plotted as bright blue ( $< -100$ ) or bright red ( $> +100$ ).

were used in the MSMFS algorithm for each image in order to cover all the accessible size scales. To obtain circular beams for the total intensity images in CASA, we used a Gaussian smoothing script on the MSMFS images with somewhat smaller clean beams, in a way which is consistent with the MSMFS formalism. For the RM-synthesis imaging, we made each narrowband Q and U image in AIPS with a taper calculated so that the clean beam was slightly smaller than the desired circular clean beam and then convolved the images, using CONVL, to the desired circular clean beam size. A subset of these will be discussed below.

### 3. RESULTS

#### 3.1. Total Intensity and Spectral Index Images

In figure 1, we show the total intensity image of the center of the Abell 2256 field with a  $6''$  circular restoring beam. This image and the many others that follow, especially the four panel figures, have more details than can easily be seen in the letter-size pages of the printed journal. We encourage the reader who is viewing the online or pdf versions of this paper to blow up these figures to examine the finer-scale features. In figures 2 top left



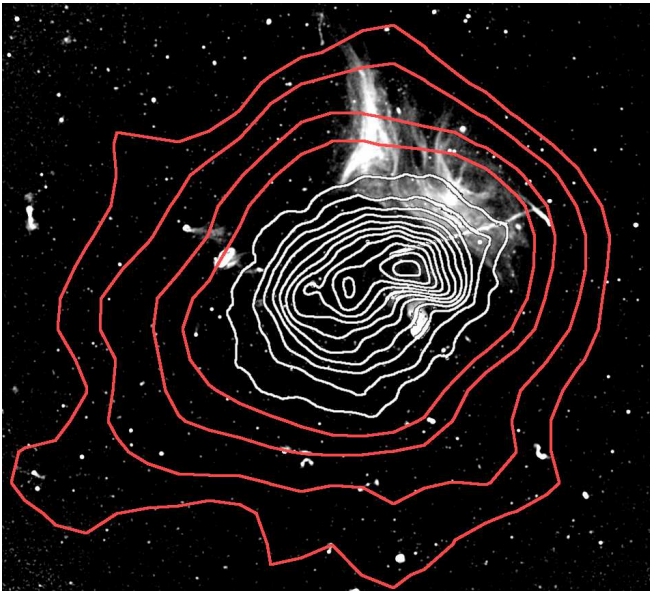


FIG. 3.— Low resolution grey scale image with 12'' resolution with X-ray overlay contours. The inner (white) contours are from *Chandra* and the outer (red contours are from ROSAT).

and 2 top right, we display the corresponding “true”<sup>5</sup> color image showing the spectral indices and their errors respectively. These images show the primary results of our total intensity imaging: the heavily filamented Large Relic; the Long Tail with a gradually steepening spectral index distribution; the central complex south of the Long Tail; the steep spectrum (red) complex to the east of the of the main concentration, consisting of a narrow angle tail source identified with a cluster member and a ring of emission not obviously attached to any cluster member; and a variety of other cluster member radio sources.

Much of the discussion of the physics of A2256 depends on the relation of the radio emission to the X-ray emission. For this perspective, we display in figure 3 X-ray contours made from a combination of the ROSAT (outer, red contours) (Briel et al. 1991) and the *Chandra* (inner, white contours) (Sun et al. 2002) images overlaid on the 12'' resolution, grey scale radio image.

### 3.2. Polarization & RM Synthesis

The polarization images shown in this paper were made using the AIPS task, AFARS, which at each pixel searches the FARS RM-synthesis cube for the maximum amplitude and outputs two RA/Dec images, one of the maximum amplitude and one of the corresponding RM. If the RM is due to a simple foreground screen then these two images are the total polarized flux density for each pixel and the RM from that screen. For this paper we will only present these results and other images derived from them using the total intensity images. In later papers we will perform a more detailed analysis.

In figures 2 bottom left and 2 bottom right, we show the fractional polarization and the peak RM for the same region as for the total intensity image in figure 1. For this RM synthesis using FARS, a range of RM from  $-200$  to

<sup>5</sup> By “true” color we mean that the color represents the measured spectral index ranging from emission relatively brighter at longer wavelengths (red) to emission brighter at shorter wavelengths (blue) as the human eye might see them if it were sensitive to radio wavelengths.

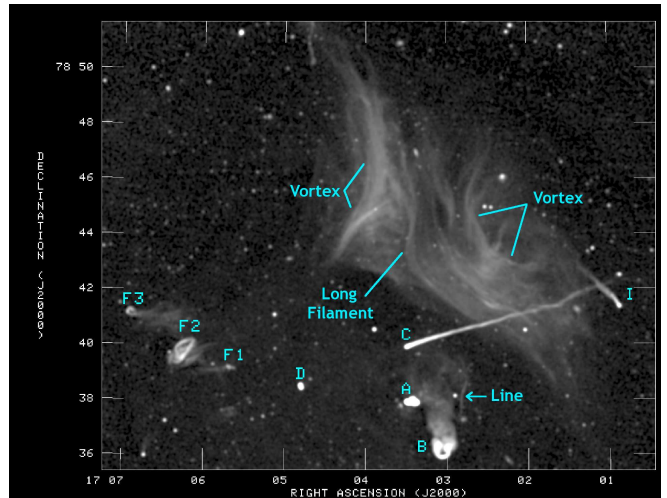


FIG. 4.— Grey-scale radio image of A2256 at 6'' resolution with source labels.

$+200 \text{ rad m}^{-2}$  was searched with a RM resolution of  $1 \text{ rad m}^{-2}$ . In practice little interesting RM structure is seen outside of the range  $-100$  to  $100 \text{ rad m}^{-2}$ , so only that range is displayed in order to show some of the RM structure without hiding the larger range of RMs visible in the field. Later in this paper we show more detail for the Large Relic and further papers will display and discuss the RM structure in detail for the other sources. For both images the polarization intensity has been corrected for noise bias and has been clipped at  $20 \mu\text{Jy}$ , about  $4\sigma$  above the noise in the AFARS maximum amplitude image. Fainter features can be seen at lower S/N along with a larger number of spurious detections. At higher resolution and with a more limited search range in RM, some of the additional structure becomes more significant.

### 3.3. Large Scale Features

In this section we will discuss the brighter, extended individual sources and source complexes. A later paper will discuss the population of 61 radio emitting cluster members found so far on the total intensity images, the most sensitive of which has 3'' resolution and an rms noise near its center of  $3.7 \mu\text{Jy}$ . Other papers will also discuss in more detail most or all of the sources in this section but the initial findings are summarized here. In figure 4, we display a smaller field containing all the cluster features we discuss below. The traditional letter designation is shown for the brighter individual sources (e.g., Miller, Owen & Hill 2003). What we will call the “Large Relic” is the large complex structure which dominates the upper part of figure 4.

#### 3.3.1. The Large Relic

Ever since the first detailed Westerbork images of Abell 2256 were produced (Bridle et al. 1979), the diffuse radio structures north of the cluster center have been a puzzle for astronomers. The most detailed study and the current standard model for the Large Relic was produced by Clarke & Ensslin (2006). Their argument is that the Large Relic is due to an outward moving shock, resulting from a cluster-cluster merger, which is located on the near side of Abell 2256. The new wide-band VLA images allow us to revisit their conclusions.

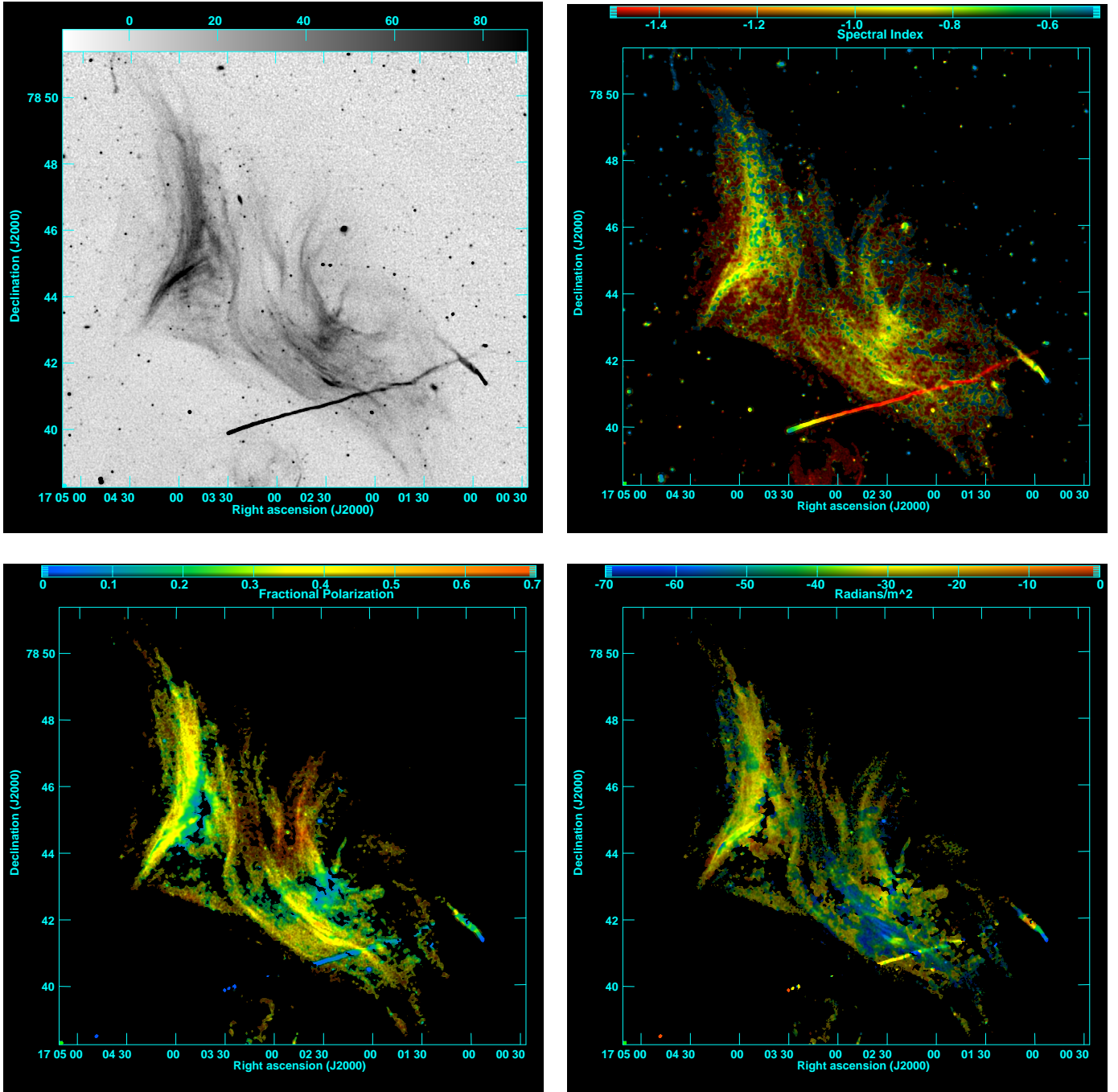


FIG. 5.— The Large Relic: Top left: Large Relic at  $3''$  resolution. The wedge at the top of the figure shows the intensities from 0 to  $90\mu\text{Jy}/\text{beam}$ . Top right: Relic true color image at  $3''$  resolution for I,  $6''$  resolution for the spectral index,  $\alpha$ . Lower left: Large Relic Intensity I-pol at  $3''$  resolution; color: Fractional Polarization,  $6''$  resolution. Lower right: Large Relic Intensity: I-pol,  $3''$  resolution; color: RM max,  $6''$  resolution.

The radio emission from the Large Relic has been called filamentary (Clarke & Ensslin 2006; Brentjens 2008) but what that means depends strongly on resolution. Generally, observations agree that the Large Relic does not have an extremely steep spectrum, e.g. spectral index,  $\alpha = -0.81, (S \propto \nu^\alpha)$  from 63 to 1369 MHz (van Weeren et al. 2012a), although Clarke & Ensslin (2006) find a mean spectral index from 1369 to 1703 MHz of  $-1.2$ . A gradient toward flatter spectral indices is also reported from southeast to northwest (Clarke & Ensslin 2006; Kale & Dwarakanath 2010). Clarke & Ensslin (2006) report fractional polarizations up to 0.45 and

an almost uniform RM near  $-44 \text{ rad m}^{-2}$ .

Our new observations show much more detail. In figure 5 top left, we show the new  $3''$  resolution total intensity image. The Large Relic is seen to be dominated by a complex filamentary structure. With the  $3''$  resolution we can not only see the filamentary web but can also resolve most or all of the individual filaments. The shape of the individual filaments is clearly correlated locally with other nearby filaments. The structure hints at being made up of at least one large vortex on the northwest side of the Large Relic, and possibly another on the eastern edge. Our highest 1-2 GHz resolution image with

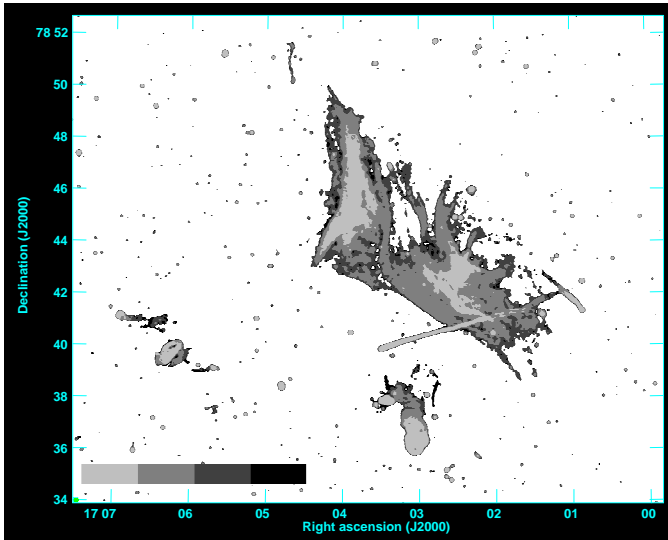


FIG. 6.— Error in spectral index for 6'' resolution for the area containing main cluster sources. Errors are given in ranges of 0.0–0.1, 0.1–0.2, 0.2–0.3 and 0.3–0.4 as shown in grey-scale wedge in the bottom-left of the figure.

a clean beam of  $2.15'' \times 1.46''$   $\text{pa} = 92^\circ$  allows us to resolve the widths of all the filaments. The smallest transverse widths are  $\sim 5''$  in projection. The long filament with a center near  $17^{\text{h}}03^{\text{m}}25.9^{\text{s}}$ ,  $78^\circ43'02''$  appears to be a twisted ribbon  $\sim 5''$  in width, which implies the Large Relic is at least 25 kpc thick.

In figure 5 top right, we show a “true color” image of the Large Relic using the L-band (1–2 GHz) spectral index image at 6'' resolution to color the 3'' total intensity image. The overall intensity weighted spectral index, excluding bright confusing sources and source C, we measure to be  $-0.94$ . However, the Large Relic is made up of a complex of different values of  $\alpha$ , typically varying from about  $-0.6$  to  $-1.4$ .<sup>6</sup> These spectral indices are flatter than those reported by Clarke & Ensslin (2006) and closer to the lower frequency measurements. One can see the spectral index gradient reported by (Clarke & Ensslin 2006; Kale & Dwarakanath 2010); however, the more striking correlation is with the most dominant bright filamentary structures, which have spectral indices near  $-0.8$ . The lower brightness regions generally have the steepest spectra. The ends of the filaments on the northern side have the flattest spectra but there are also very steep regions in the northwest and on eastern edge as well. We show in figure 6 the estimated errors in the 6'' resolution spectral index image.

We display in figure 5 bottom left a color image of the same 3'' total intensity image but in this image the color is the fractional polarization from the 6'' resolution AFARS amplitude image divided by the 6'' resolution total intensity image. The bright total intensity filaments show a high fractional polarization, typically 0.3–0.4. These levels confirm the generally ordered underlying magnetic fields in the filaments that one would guess from the total intensity image. The filaments in the north-central part of the Large Relic stand out as having having even higher fractional polarization, up to

<sup>6</sup> The fine scale color structure in this image is at least partly due to the noise in the spectral index at 6'' resolution. However, one can see the general trends better at this higher resolution than in figure 2.

0.7. These same filaments show the flattest radio spectra. On the other hand, there are regions, especially in the northwest, which show signs of disorder with  $\lesssim 0.2$  fractional polarization.

Thus, when the Large Relic is observed in more detail, the simple gradient from north to south in spectral index does not dominate the picture. Perhaps our new, more detailed images suggest that the most recent particle acceleration is associated with the flat spectrum filaments with well-ordered fields on the north side of the relic.

In figure 5 bottom right, we display a color figure of the peak RM from AFARS. The total intensity and field of view are the same as for the previous two figures but this time the colors are the RMs at the peak polarized amplitude. This image, as well as figure 5 bottom left, was produced using a narrower search range in RM ( $-70$  to  $0$   $\text{rad m}^{-2}$ ) and a lower  $4\sigma$  cutoff ( $10\mu\text{Jy/beam}$ ) after correcting for noise bias. The higher resolution and smaller range of RM allows the lower cutoff than in figure 2.

This RM image shows a pattern in the Large Relic not clearly correlated with the total intensity. There are relatively large, coherent patches of Rotation Measure up to a few arcminutes in size, typically ranging from about the galactic foreground value,  $-25$   $\text{rad m}^{-2}$  down to about  $-70$   $\text{rad m}^{-2}$ . These patches show much larger deviations from the mean than is consistent with studies of either Galactic RM fluctuations (Schnitzeler et al. 2009) or the local Galactic RM gradient across the Abell 2256,  $\sim 10$   $\text{rad m}^{-2}$  per degree (Brentjens 2008).

Clearly, the RM is not almost constant across the Large Relic, as appeared to be the case at the S/N and resolution of Clarke & Ensslin (2006). The RM values are not greatly different than those seen from other cluster members in figure 2 bottom right. Whether the more negative RM values are from the cluster or are local to the relic is unclear from these data. A more detailed analysis of the polarization associated with the Large Relic will be made in our subsequent paper.

Another hint to the nature of the Large Relic is shown in the high contrast total intensity image in figure 7 left. One can see that the four sides of the Large Relic have almost sharp boundaries in a shape like a parallelogram. Some physical process must be creating these sharp boundaries.

Certainly the Clarke & Ensslin (2006) model for the Large Relic, as an outgoing shock on the near side of the cluster, is not ruled out by these results. However, some of the arguments for their model are weakened. The X-ray images do not, as yet, show any evidence of a shock coinciding with the Large Relic (Sun et al. 2002; Bourdin & Mazzotta 2008; Kale & Dwarakanath 2010). In addition, the Clarke & Ensslin (2006) picture relied on the low level of RM dispersion they detected across the relic, which was much smaller than the value they expected if the relic were behind the cluster (based on their model of the intracluster medium). Our new observations, however, reveal more significant RM variations across the relic, and also show that the RM values across the relic are comparable to those seen in other cluster members. Thus the RM data no longer require the relic to sit on the near side of the cluster. Perhaps other models should be considered, such as a large-scale current sheet between two magnetic domains.



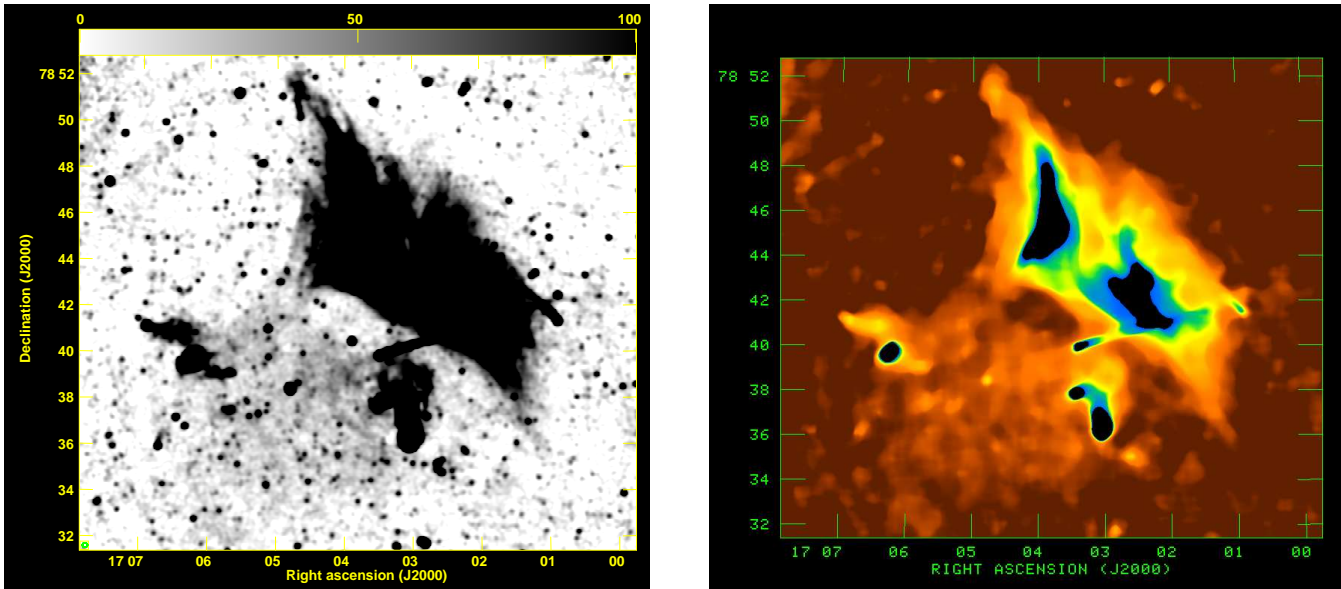


FIG. 7.— Large Scale Structure. Left: Saturated 12'' resolution image showing “parallelogram” outer 4 sharp edges of the Large Relic. Right: Deep TVHUE Median Window Filter Lowpass image. This image shows the connection between Large Relic and the Halo near the F complex.

### 3.3.2. The Halo and Larger Scale Features

Several papers report on the properties of the very diffuse emission south of the Large Relic, which is called the Halo (Clarke & Ensslin 2006; Brentjens 2008; Kale & Dwarakanath 2010; van Weeren et al. 2012a). No polarization is detected and a steep radio spectral index is found,  $\lesssim -1.5$ . These properties are generally consistent with the class of objects called “halos” in rich clusters (Feretti et al. 2012). Thus most papers assume Abell 2256 has both a halo and one or more relics which are generally considered separately.

Low frequency results have recently been reported from Westerbork (Brentjens 2008; van Weeren et al. 2009), the GMRT (Kale & Dwarakanath 2010), and from LOFAR (van Weeren et al. 2012a). The observations reported here were not designed to focus on the very diffuse features which could be studied in detail with the upgraded VLA either with more integration time in the D-configuration or perhaps lower frequency data with the new Lowband system. However, our combination of resolution and sensitivity shows one interesting large scale, low surface brightness feature. In figure 7 right we show a median window filtered image of our 12'' resolution image. This image shows a connection between the Large Relic and the Halo (the diffuse feature south of the large relic) along a curved arc on the eastern boundary of both features. The arc also connects the Large Relic and the Halo near complex F which we will discuss next. It appears as if the eastern boundaries of the Halo, the Large Relic, their connection and possibly the F complex have some common cause, although no related structure can be seen in existing X-ray images.

The large scale structure of Abell 2256 is hard to understand because of the fundamental problem of translating a two dimensional image to three dimensions. The Large Relic has been suggested to be a relatively thin structure in the plane of the sky which we see projected onto the X-ray, supposedly, three dimensional structure. However, the Large Relic and the large, curved arc are seen in two

dimensions near an outer the edge of the bright *Chandra* X-ray emission region, see figure 3. So either the Large Relic and the arc in three dimensions are bounded by the dense cluster cluster gas, or they lie well outside of the central cluster region and are seen in projection by chance against the X-rays. The Large Relic itself has structures on the eastern and north-western side which could be interpreted as being vortices seen in projection. This could suggest that the Large Relic is not a thin sheet but has some depth along the line-of-sight. In any case the relic and the arc are outside of the region of high X-ray S/N and thus we know little about the structure of the gas in these regions.

The comparison with other relics is difficult. Most “relics” are elongated, “fuzzy” patches without an obvious optical identification associated with a relatively distant cluster of galaxies (e.g., Feretti et al. 2012). A few sources, characterized as “round relics” by Feretti et al. (2012) could be similar to the structure in Abell 2256 but the size and radio luminosity of most of these sources are very different from our case. One such source associated with Abell 1664 is very similar (Govoni et al. 2001) and a few others with better radio imaging might be in the Abell 2256 class. However, the current radio observations which have been used to search for relics and halos are mostly too low in resolution to distinguish sources like the Large Relic from halos and other types of diffuse emission. Thus the class of Abell 2256-like relics remains to be cataloged. Clearly such diffuse sources with similar sizes in two dimensions on the sky and relatively high surface brightness are unusual.

### 3.4. Radio Complexes and Individual Sources

#### 3.4.1. Steep-Spectrum Complex F

On the eastern edge of the cluster radio emission is a complex of sources: Complex F. All the previous observations of Abell 2256 have discussed this source since it is fairly well separated from the other radio structure and shows a a very steep spectrum. Röttgering et al. (1994) report the shell structure of F2 but do not clas-



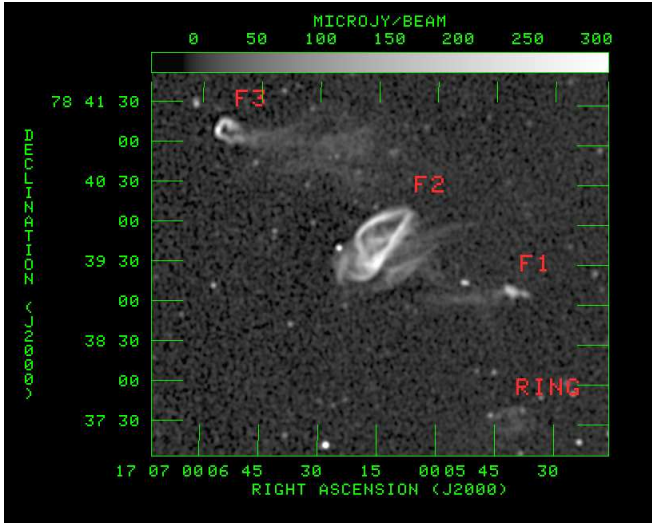


FIG. 8.— Large F region including ring galaxy at 3'' resolution.

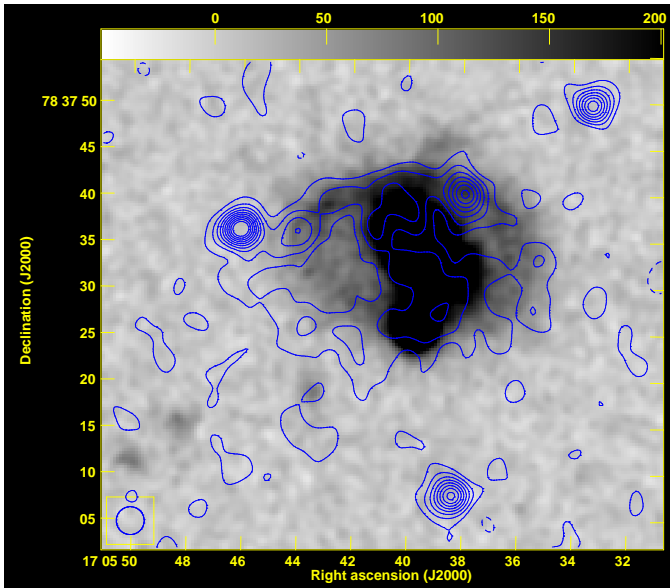


FIG. 9.— Radio/Optical ring galaxy overlay. Grey scale is R SDSS image convolved with a 1'' FWHM circular Gaussian. Contours are  $1.5e-5 \times (-1, 1, 2, 3, 4, 5)$  Jy/beam. Radio resolution is 6''.

sify F3 as a Narrow Angle Tailed radio galaxy (NAT, as defined by Owen & Rudnick (1976)) since they assume that the whole complex is an unusual “Z-shaped” single source. For F2, Brentjens (2008), Kale & Dwarkanath (2010), and van Weeren et al. (2012a) report spectral indices over the range from 63 to 350 MHz  $\sim -1.2$  and between 350 and 1450 MHz  $\sim -1.8$ . Clarke & Ensslin (2006) measure  $-2.5 \pm 0.2$  between 1369 and 1703 MHz and also find fractional polarization  $< 0.02$ .

In figure 8 we show a grey-scale image of four radio sources in this region at 3'' resolution with labels. Source F3 is a clear NAT associated with a cluster galaxy at its far eastern edge. F2 and F1 do not have clear optical/NIR identifications. The source labeled RING is an optical ring galaxy (Abazajian et al. 2009)[hereafter, SDSS] with associated radio emission (figure 9) which may not have anything to do with F1, F2 or F3 but is located in the same general region.

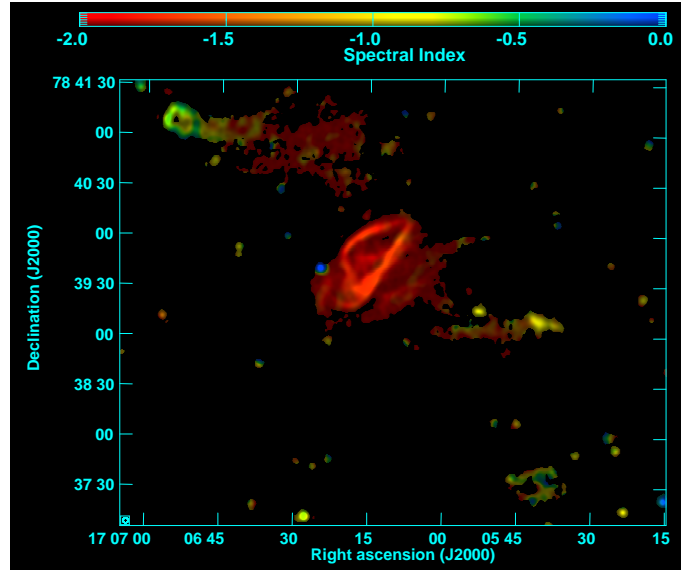


FIG. 10.— True Color image of region F, total intensity at 3'' resolution, spectral index. at 6'' resolution. Individual sources F3, F2, F1 and the Ring galaxy are labeled in Figure 8.

In figure 10 we show a true color image of the complex showing that all three components have very steep spectral indices. Our image shows the spectral index structure for the entire complex between 1 and 2 GHz. For F2 we see typical values in the bright part of the ring of  $\sim -1.8$  and the intensity weighted spectral index for F2 is  $-1.85$ . Thus we do not find that F2 is steepening in spectral index between 1 and 2 GHz in comparison with the values found at lower frequencies. For F3 we see spectral indices near the parent galaxy  $\sim -0.7$  increasing to more uncertain values near  $-1.5$  down the tail. For F1 we find values that range from  $\sim -1.4$  to  $\sim -0.8$  near its western end. While the connection of F1, F2 and F3 is unclear, it is very unusual to find three such large, unusual morphology, steep radio spectrum sources in so small an area on the sky. Source F3 is a fairly normal NAT. F2 is very unusual. It has no good candidates for an optical identification but does have an inverted spectrum point ( $393\mu\text{Jy}$ ,  $17^{\text{h}}6^{\text{m}}24.97^{\text{s}}$ ,  $78^{\circ}39'41.0''$ ) with a spectral index  $\sim +0.6$  in the 1-2 GHz band, seen as a blue dot in figure 10, which appears to be attached to one of F2's red filaments. No optical object is near the blue dot in SDSS images, but there is a WISE (Wright et al 2010)  $3.3\mu\text{m}$  and  $4.6\mu\text{m}$  detection  $\sim 0.5''$  from this position. F3 looks like it might be part of a normal tailed radio galaxy but there is no optical identification to the limit of the SDSS coincident with the radio emission. Unlike the lower spatial resolution results of Clarke & Ensslin (2006), at 6'' resolution, around the bright ring we see fractional polarizations ranging from  $< 0.02$  to  $0.15$ . For approximately 10 independent beams showing strong polarization, the RMs vary from  $\sim 0$  to  $-300$  rad  $\text{m}^{-2}$ . Even larger values of  $\text{abs(RM)}$  are likely present, but a more thorough analysis of the errors is required to establish their reality. Thus at our higher resolution F2 is polarized and has a range of RM values which could have depolarized the source at the lower resolution of Clarke & Ensslin (2006).

Except for F3, which clearly has an optical identification with an Abell 2256 member galaxy, the rest of F

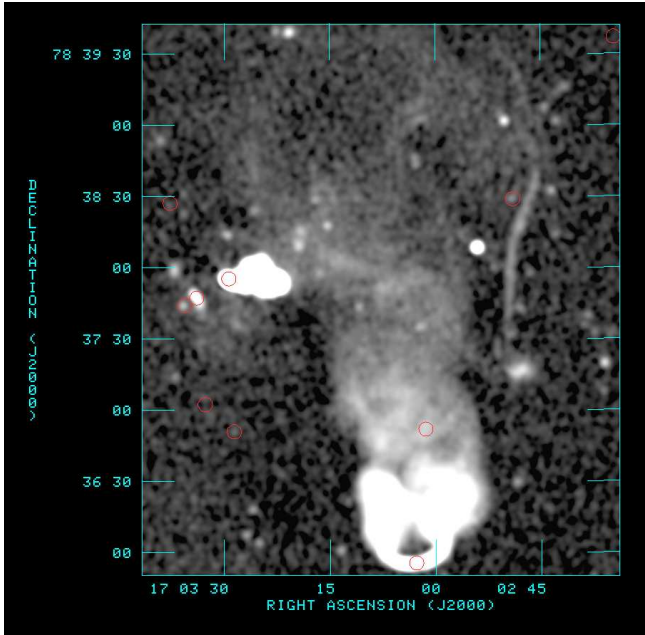


FIG. 11.— A+B region 3'' resolution. Red circles mark locations of cluster members with measured redshifts. Individual sources A, B and the Line are labeled in Figure 4.

could be one or more background sources seen by chance in the cluster field. The existence of the point source with an inverted radio spectrum associated with a WISE source also could be a random background source superimposed on F. The lack of an SDSS counterpart to this point source certainly is consistent with a dusty, perhaps high redshift, galaxy. F1 and F2 could be associated with this object. However, given the current data, the existence of such an unusual morphology, very steep spectrum, large background source very close to a NAT radio galaxy which also has an unusually steep spectrum radio tail seems like too big a coincidence to call F2/F1 a background source. It also seems possible that the WISE source is a very dusty galaxy in Abell 2256. We will have to hope that future observations make the situation clearer.

Perhaps the object most similar to F which has been discussed extensively is the NGC1265 complex in the Perseus cluster. That galaxy has a NAT radio source with an apparently attached, steep-spectrum ring (Sijbring & de Bruyn 1998). Pfrommer & Jones (2011) modeled the ring as a bubble of gas passing through a cluster shock. The F3/F2 complex seen from a slightly different angle might be a similar structure. Since the F complex lies near the apparent boundary with the large-scale radio arc (figure 7) these sources could have a similar origin. The fact that the F-complex is a second example of structure similar in morphology to NGC1265 and its adjacent ring may suggest a more direct connection between mass loss from the radio galaxy and the process responsible for the ring than suggested in the “radio phoenix” model of Pfrommer & Jones (2011).

An interesting, related question is whether some or all of the F-complex should be considered a “relic” since it has a very steep radio spectrum, is polarized, and is an elongated structure on the outskirts of the cluster.

### 3.4.2. Central A/B Complex

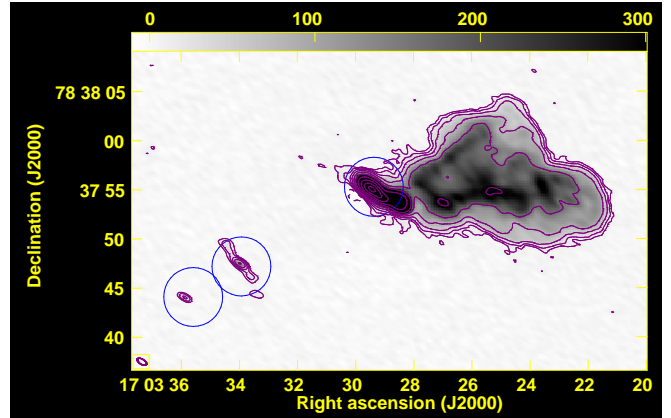


FIG. 12.— Source A: Grey scale with contours at S-band. Clean beam= $1.07'' \times 0.51''$   $\text{pa}=57^\circ$ . Contours are  $10 \times (-1, 1, 2, 4, 8, 16, 32, 64, 128, 256) \mu\text{Jy}/\text{beam}$ . The intensity wedge at the top is in units of  $\mu\text{Jy}/\text{beam}$ . The blue circles are 3'' in radius and show the locations of three galaxies in the NGC6331 triple system.

Near the center of the field below the Large Relic is the A/B Source Complex. Figure 11 is a grey-scale image of the complex including a large NAT (source B) running from the bottom of the figure at least half way to the top. Source A is the small, very bright, extended blob to the east of source B. Earlier work at 1400 MHz with the VLA (Röttgering et al. 1994; Miller, Owen & Hill 2003) showed the horseshoe-shaped morphology of B, characteristic of a NAT. Recent images at frequencies below 1 GHz (Brentjens 2008; van Weeren et al. 2009; Kale & Dwarakanath 2010; van Weeren et al. 2012a), show that there is complicated, steep-spectrum structure along the northern extension of B.

Our new images show more details. At the top of source B (or just above it) there is perhaps a faint ring and/or some other fine-scale structure covering the upper half of the image. To the west of B there also are one bright “Line” and perhaps another fainter line above it. In the upper left panel of figure 2, one can see that source B shows a steepening spectral index like most NATs (e.g., Sijbring & de Bruyn 1998; Lal & Rao 2004) as well as a very steep spectrum region corresponding to what is seen on the lower resolution, lower frequency images (Brentjens 2008; van Weeren et al. 2012a). It is not clear whether this region is part of B, part of a separate ring or in some way related to A. The Line, not clearly seen in the lower frequency images, also has a very steep spectrum and is  $\sim 40\%$  polarized.<sup>7</sup> Perhaps the Line is part of the steep spectrum region north of B. Our new imaging raises the question of whether all the steep spectrum structure in the northern half of the complex is part of B or one or more distinct emission regions projected as if they were connected with B. In figure 3, the X-ray overlay, one can see a strong gradient in the X-ray emission which is a cold front (Sun et al. 2002) slightly to the north of the steep spectrum radio bar and just south of the ring. Is this radio structure somehow related to the cold front?

In figure 12, we show the S-band (2-4 GHz) A-configuration image of source A and friends, with contours overlaying the grey-scale. The optical identifica-

<sup>7</sup> The slightly extended blob below the Line is associated with a galaxy which is not a cluster member.

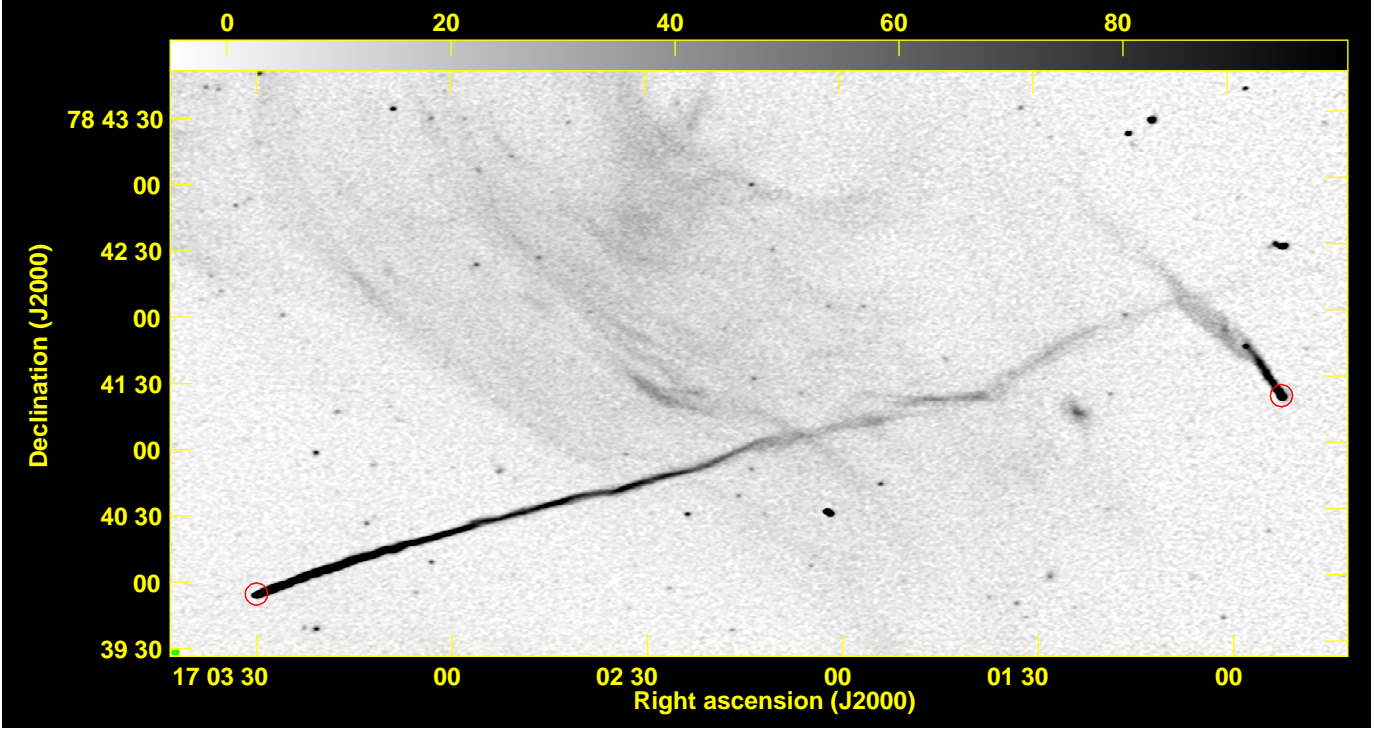


FIG. 13.— Sources C and I at L-band full resolution with optical IDs (red circles). Clean beam= $2.15'' \times 1.46''$   $pa=92^\circ$ . The green circle showing the beam is in the lower left corner of the image.

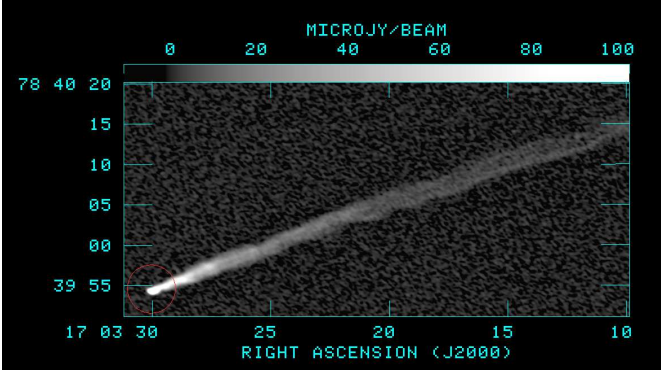


FIG. 14.— Source C head in 4-6 MHz band with  $3''$  radius red circle on optical ID. Clean beam= $0.57'' \times 0.34''$   $pa=64^\circ$ .

tion of A is apparently part of a triple galaxy, which as a unit should probably be called NGC6331 based on the NGC catalog (Dreyer 1888), which is the only NGC galaxy and the brightest galaxy in the cluster. The entire system appears to be contained in a single diffuse optical halo on the SDSS *r* image with a major axis  $> 70$  kpc in diameter. In our image one can see radio emission from all three components of the triple, which have a range of radial velocities of 1728 km/s (Berrington, Lugger & Cohn 2002), not unusual for such a multiple system but likely indicating that the individual components are on highly radial orbits that pass near the core of the cluster (Tonry 1985a,b). The radio galaxy A was included in the original list of six NATs by Rudnick & Owen (1976). Röttgering et al. (1994) also describe A as a definite head-tail source (i.e. a NAT). However, source A has a much higher surface brightness than any other radio galaxy in the cluster and the sharp boundaries of the radio source seems to indicate a source more like a bubble than a tail. Source A appears to be small on the

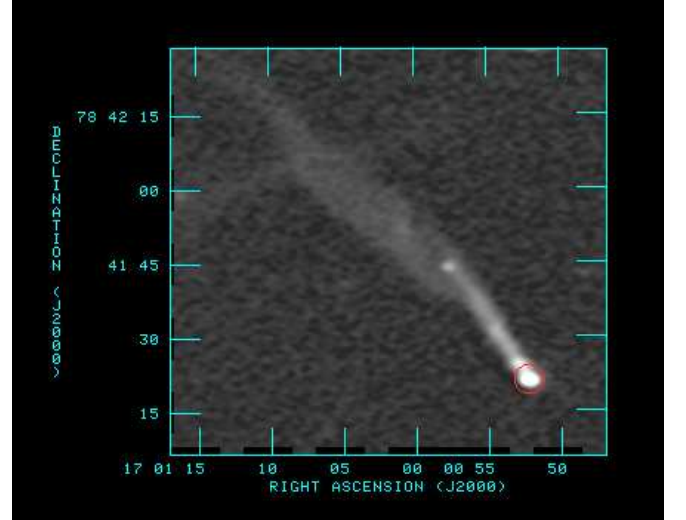


FIG. 15.— Source I: L-band Clean beam= $2.15'' \times 1.46''$   $pa=92^\circ$ . The red circle shows the location of the center of the optical identification.

cluster scale; however, it is useful to compare A with the central cluster radio source associated with M87 (e.g., Owen, Eilek & Kassim 2000), a buoyant bubble blown in the cluster gas at the center of the Virgo Cluster (e.g., Churazov et al. 2001). The major axis of A is  $\sim 31$  kpc in size, about half the full size of M87 radio source. Its 20cm luminosity is  $1 \times 10^{24}$  W  $\text{Hz}^{-1}$ , about 7 times smaller than M87; however, the brightness per unit volume is very similar. One can see a double structure in figure 12 on the eastern side of the source, about 5 kpc in size, very similar to the inner double in M87 (e.g., Hines, Owen & Eilek 1989). Thus, except for the offset structure of the bubble, the parameters of source A seem more similar to a central cluster bubble than a NAT.



### 3.4.3. The Long Tail C and tail I

Perhaps the second most striking feature in the cluster is the Long Tail, source C. VLA images of both C and I are reported by Röttgering et al. (1994) and Miller, Owen & Hill (2003) at 1400 MHz and at 325 MHz by Röttgering et al. (1994). In particular Röttgering et al. (1994) considers the Long Tail C as a NAT. They show that the source remains straight and unresolved along much of the tail and that the spectral index steepens along the tail. They conclude it is likely not a jet since it doesn't show a clear nuclear component and because most low luminosity jets are two-sided. They then consider the problem of how a trail produced by a galaxy orbit could follow the observed, straight path. They conclude that such an orbit is possible if the initial velocity is two or three times higher than the cluster velocity dispersion, the galaxy orbit is well outside the merging region, and the bent-back, twin jets at the galaxy nucleus are hidden by their  $1.2'' \times 1.4''$  resolution.

In figure 13 we show the grey-scale image at the full L-band (1 – 2 GHz) resolution. On our images source C is  $\sim 540$  kpc in length in projection. The tail could be  $\sim 800$  kpc long if the steep spectrum features, AG+AH, are part of the tail (van Weeren et al. 2009, 2012a). Also plotted in the field is source I and the positions of the optical identifications are shown as small red circles. Note that C wiggles and perhaps interacts with the Large Relic but doesn't show split trails. However, in figure 14 we display the 4-6 GHz, A-configuration image of the head of C at  $\sim 0.5''$  resolution. Here we see the bright core and some bifurcation of the tail downstream but not near the central component. In fact the “trail” emission seems more to be limb brightened and to show twisted filaments like many radio jets, e.g. M87 (Owen, Hardee & Cornwell 1989). Near the core the source has only one strand and is  $\lesssim 100$  pc in diameter, based on a fit to the 6-8 GHz image which has a resolution  $\sim 0.3''$  across the inner part of the source. Thus we do not see the bifurcation expected near the core of the twin, bent-back jets normally seen in Narrow Angle Tail sources. Apparently the Long Tail could be a one-sided jet. Perhaps the other side of the twin jet has been disrupted by the ram pressure due to the motion of the galaxy relative to the cluster IGM or perhaps the limb brightening we see is an indication of an underlying twin tail structure. If so, the bending of the twin tails must take place very deep in the galaxy core where one might expect little impact from the galaxy's motion through the IGM, unless the galaxy has been almost completely stripped.

In figure 15, we show the S-band image of source I. Close to its parent galaxy source I also seems to be primarily a one-sided jet. At the end of the inner part of the “tail” there is a “knot” or perhaps a “hot-spot”, just before the tail changes direction and becomes more of a diffuse plume as seen in figure 13. This morphology certainly resembles a jet ending in a hot-spot. The direction of the more diffuse structure beyond the knot then changes, suggesting that the relative velocity vector of the external medium is not along the direction of the inner structure. Perhaps not all NATs cited in the literature are twin jets bent back by ram-pressure. In these two cases if the direction of the “trail” is related to the motion of the galaxy relative to the external medium,

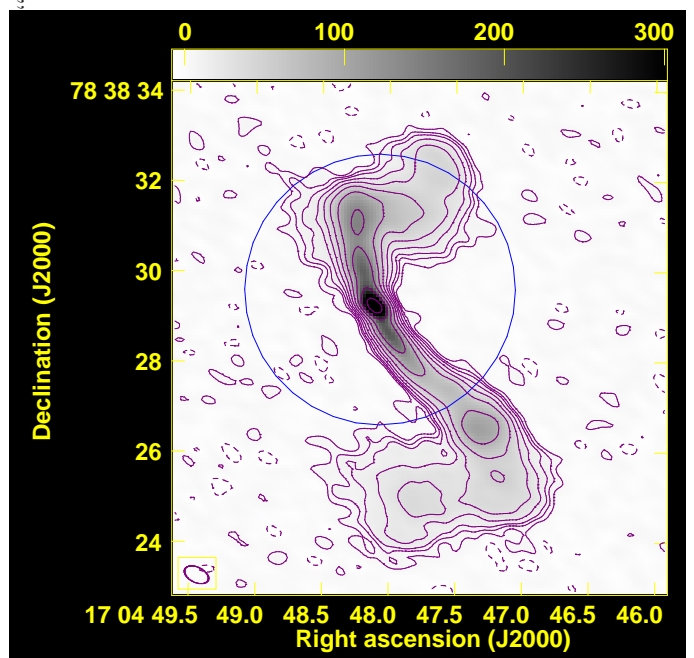


FIG. 16.— Source D: 4 – 6 GHz image with circle for optical. Contours are  $4 \times (1, 2, 3, 5, 8, 13, 21, 34, 55, 89, 144) \mu\text{Jy}/\text{beam}$ . The intensity wedge at the top is units of  $\mu\text{Jy}/\text{beam}$ . Clean beam =  $0.57'' \times 0.34''$   $\text{pa} = 64^\circ$ . The  $3''$  blue circle shows the location of the optical galaxy.

the second jet has not remained stable.

Sources C and I raise the interesting question of whether single thin structures that appear similar to one-sided jets can actually be tails swept back by the relative motion through the ICM, similar to the twin-tailed NATs. In this case, the question remains whether only a single jet was launched from the AGN, or whether a second jet was launched, but quickly disrupted. VLBI observations of apparently single tails might resolve this issue.

### 3.4.4. Source D

Röttgering et al. (1994) show an image of source D and the location of its parent galaxy suggesting it is not located near the galaxy center. In figure 16 we show a grey-scale plus contour plot of source D, made at S-band in the A-configuration. The  $3''$  ( $\sim 3$  kpc) radius blue circle marks the centroid of the optical galaxy based on the SDSS image. This FRI is entirely contained within the isophotes of the optical galaxy. The galaxy is almost centered on the core of the radio source emission.

## 4. DISCUSSION

Abell 2256 is perhaps the most striking collection of radio structures in a rich cluster. Why is that? Abell 2256 is a fairly rich cluster, Abell richness class 2, but clearly less rich than Coma, which is almost richness class 3. Coma possesses a radio halo and several radio galaxies but seems dull in appearance compared to Abell 2256. Perhaps the objective reason for the appearance of Abell 2256 is the surface density of complex radio emission. But why is there so much going on?

In this paper we have presented more detailed observations of many of the sources than have previously been published. Many show unusual properties. Certainly the relatively flat-spectrum Large Relic takes up the most



surface area. While there are other sources called relics which are as luminous and have as large a linear extent in one dimension, we are unaware of such a large two-dimensional area of emission with an average spectral index at 20cm near  $-0.9$ . Certainly there must be other such sources but apparently not so nearby. There are also several very steep spectrum extended regions of radio emission. Most prominent are the F-complex, the Line, and the ridge at the top of Source B. Except for the NAT, F3, none of these sources have obvious optical identifications. Along with the Large Relic these sources seem to be non-AGN “cluster sources”. The Long Tail, source C, which could be a very long, one-sided jet, is also unusual if not unique.

#### 4.1. *Abell 2256, an off-axis, mid-merger event ?*

What physical properties of Abell 2256 could be responsible for this collection of unusual radio structures? Certainly the mass, X-ray luminosity and the cluster temperature are not unusual. However, in addition to the apparent three groups in the galaxy velocity space, the *Suzaku* observations of Tamura et al. (2011) show that the two peaks in the X-ray image in figure 3 differ in radial velocity by  $\sim 1500 \text{ km s}^{-1}$  so there is strong evidence for a very active merger. Vijayaraghavan & Ricker (2013) have recently reported a simulation of a group-cluster merger which may provide a context for understanding Abell 2256. This simulation shows that special, extreme conditions occur close to the time when the group passes close to the centroid of the larger cluster. The relative velocity of the galaxies in the group with respect to the cluster galaxies and the external medium reaches a maximum about three times greater than for galaxies in a similar isolated cluster. The simulation also shows that the ram pressure on the galaxies, especially those in the group, increases by up to two orders of magnitude (supposedly due to relative motion of gas and galaxies). The interaction of the ICM in the group with the larger cluster transfers energy to the cluster ICM in the form of shocks, flows and general heating. This interaction has the potential to create new boundaries in the external gas which could be seen in radio emission.

Other simulations of mid-merger conditions also produce interesting insights into possible physical conditions in Abell 2256. In particular, Takizawa (2000), Roettiger, Stone & Mushotzky (1998) and Ricker & Sarazin (2001) simulate slightly off-axis mergers which produce complex, asymmetric conditions especially near mid-merger. Takizawa (2000) and Ricker & Sarazin (2001) both show that at times close to mid-merger there are isolated high temperature regions which wrap around parts of the outer boundaries of the two X-ray intensity peaks. Roettiger, Stone & Mushotzky (1998) show similar results tuned to match the X-ray results for Abell 754 but also show the velocity field in the gas and the location of the group ICM relative to the X-ray brightness. This simulation shows that the unseen, heated group gas is flowing toward the brightest X-ray peak, creating a sharp boundary and a weak shock. While these simulations should not be expected to duplicate Abell 2256, they suggest that part of the Abell 2256 morphology could be due to an off-axis merger.

Based on comparing the Takizawa work with the *Chandra* X-ray observations, Sun et al. (2002) concluded that

Abell 2256 is seen in mid-merger. The detailed line-of-sight galaxy velocities also seem consistent with that possibility. Berrington, Lugger & Cohn (2002) report three distinct statistical, velocity/spatial groupings in Abell 2256: a primary cluster with 186 members, a large infalling cluster with 78 members and a group with 30 members. These results seem consistent with Vijayaraghavan & Ricker (2013). In particular, near mid-merger the simulation shows that the group splits into two velocity components, in addition to the remaining main cluster distribution. Whether there are two or three mass components the overall picture is consistent with Abell 2256 being seen at mid-merger and in a not quite head-on merger. Also, interesting interactions are likely going on the edges of the main X-ray emitting brightness distribution.

This leads to possible interpretations of the source C, and perhaps source I, as due to the much increased ram pressure on the group members and relative velocities between the group members and the cluster gas. The simulation of Vijayaraghavan & Ricker (2013) shows that the ram pressure can rise above  $10^{-10} \text{ dyne cm}^{-2}$  close to mid-merger. Their models show the pressure is high enough to completely strip galaxies, in agreement with Gunn & Gott (1972) and the more detailed stripping simulations of Roediger & Brüggen (2006).

The F complex lies  $\sim 500 \text{ kpc}$  in projection from the center of the cluster near a boundary shown in figure 7 beyond the edges of the bright X-ray emission in figure 3. Perhaps this suggests that these features are related to lower density gas flowing toward the main cluster reservoir stripping the galaxy associated with F3. Vijayaraghavan & Ricker (2013) also show that the mid-merger interaction between the group and the cluster increases the cross-section for galaxy collisions, which could be responsible for the ring galaxy near the F complex shown in figure 9. These unusual radio galaxies may be showing us that the increased ram pressure at mid-merger dominates the stripping and thus the evolution of cluster galaxies, rather than the interactions during the much longer, benign phases of a cluster’s life.

Thus while the discussion above is far from definitive, the off-axis mid-merger hypothesis has aspects that could be responsible for origin of the large number of unusual features seen in Abell 2256. If this hypothesis is correct, studies of other mid-merger clusters in detail, looking for similar phenomena, offer a new way to investigate the evolution of clusters and the galaxies in them.

#### 4.2. *The Large Relic Physics*

Radio relics on the outskirts of clusters are typically interpreted as cluster merger shocks, which are radio-loud due to in situ particle acceleration; the Large Relic in Abell 2256 has specifically been interpreted this way (Clarke & Ensslin 2006). However, this object does not fit easily into the simple picture, for several reasons.

1. The Large Relic has an unusually large aspect ratio, being nearly as wide as it is long. Most other, well studied relics are long, thin structures, no more than  $\sim 100 \text{ kpc}$  wide (e.g. the “sausage” relic van Weeren et al. 2010, or the “toothbrush” relic, van Weeren et al. 2012b); similar widths are predicted by theoretical models (e.g., Kang et al. 2012; Skill-

man et al. 2013).

2. The Large Relic is polarized at significant levels, which suggests large-scale ordering of the magnetic field in the sky plane. It also has large, coherent Rotation Measure patches, which suggests large-scale ordering of the magnetic field along the sight line. By comparison, merger-shock models predict the magnetic field will show disorder on small scales in the shock plane (e.g., Skillman et al. 2013); thus the relic should be polarized only when viewed edge-on.
3. It is not clear that the relatively weak merger shocks (Mach number  $\sim 2 - 3$ ) expected from simulations can account for radio-loud structures such as the Large Relic. Much stronger shocks are probably needed in order to accelerate a significant number of electrons from the thermal pre-shock plasma and amplify the pre-shock magnetic field to useful levels (e.g., Gieseler et al. 2000; Brunetti & Jones 2014). Alternatives such as reacceleration of fossil cosmic-ray electrons (e.g., Pinzke et al. 2013) are challenged by the need to have a pre-existing Mpc-scale fossil structure. Furthermore, no evidence for such a shock close to the large relic has yet been found in the X-ray data on this cluster (Sun et al. 2002; Brentjens 2008).

These arguments do not, of course, preclude the Large Relic being an unusual example of a merger shock. That model is still worth consideration, but we also want to explore alternative models. One such class of models would have the Large Relic being the result of a large-scale current sheet, sitting at the boundary between two magnetic domains (e.g., Priest & Forbes 2000) involved in the ongoing merger (as in, for instance, the simulations of Roettiger, Stone & Mushotzky (1998)). We will present a more detailed study of both models in a subsequent paper on the Large Relic, but a few points are worth noting here. In a magnetized plasma environment, such as the intracluster gas involved in an ongoing merger, current sheets arise naturally at plasma boundaries and also at velocity shear surfaces. Current sheets are well known to produce magnetic flux ropes when they become unstable to the tearing mode (e.g., Priest & Forbes 2000), providing a natural explanation for the dramatic filaments in the Large Relic. Magnetic reconnection across current sheets also provides an alternative source of particle acceleration. While this process is not as well understood as diffusive shock acceleration, two mechanisms have been suggested. The electrons may gain energy by falling through the large-scale potential drop in the current sheet (e.g., Romanova & Lovelace 1992; Benford & Protheroe 2008). They may also undergo first-order Fermi acceleration if the plasma converging on the reconnection region are turbulent (de Gouveia dal Pino & Lazarian 2005; Drury 2012). While neither of these mechanisms is as well-studied as is shock acceleration, both seem likely ways to make a merger-driven current sheet “light up” as a radio relic.

## 5. CONCLUSIONS

The new, high resolution, high sensitivity observations with the upgraded VLA reveal many new details about

Abell 2256.

1. The Large Relic is made up of a complex system of filaments which also show locally correlated topology. Complicated variations in spectral index,  $\sim -0.6$  to  $-1.4$  are seen across the source, with steeper spectra tending to be in lower surface brightness, less filamented regions. Fractional polarization is in the range  $\lesssim 0.1$  to  $0.7$ , and coherent patterns of Rotation Measure are  $\sim 100$  kpc in size. Essentially all the filaments are  $\lesssim 5$  kpc wide. The shapes of the filaments are correlated over  $\sim 200$  kpc. One apparently twisted filament suggests that the width of the Large Relic is at least 25 kpc.
2. An arc of low surface-brightness emission appears to connect the Large Relic with complex F and the radio halo, suggesting a physical connection between these features.
3. The steep-spectrum source, F2, is a polarized, pseudo-ring structure and doesn’t appear to be directly connected with any radio galaxy, although it has interesting similarities to the ring associated with NGC1265 which is modeled as bubble that has passed through a shock (Pfrommer & Jones 2011).
4. The northern half of the A/B complex shows a bubble-like structure, with steep spectrum, filamentary structures. The most prominent is a thin “Line” of emission west of B which has a very steep radio spectrum and a fractional polarization of  $\sim 0.4$ .
5. The relatively high surface brightness and sharp edges of source A suggest it is a bubble with more physical and morphological similarities to cluster center sources like M87 than to NAT radio galaxies.
6. The Long Tail, source C, does not show a bifurcated structure near the core, as one would expect for a radio tail, and is  $\lesssim 100$  pc in diameter. The source could either be due to extreme stripping of the galaxy’s ISM due to the cluster/group merger and/or it could be a one sided jet. Source I also shows a similar, single-strand structure near its nucleus.
7. The unusual radio phenomena seen in Abell 2256 could be due to the cluster being seen at near mid-merger of a slightly off-axis collision of a cluster and a group.
8. Given the lack of evidence for a strong shock near the Large Relic which could accelerate the relativistic electrons seen as synchrotron emission, it is worth considering other models such as reconnection between two magnetic domains.

## 6. ACKNOWLEDGMENTS

We wish to thank Eric Greisen for help with the development of several AIPS tasks and verbs used in our analysis.

Partial support for the work of LR is provided through NSF grant AST-1211595 to the University of Minnesota.

Funding for the SDSS and SDSS-II has been provided by the Alfred P. Sloan Foundation, the Participating Institutions, the National Science Foundation, the U.S. Department of Energy, the National Aeronautics and Space Administration, the Japanese Monbukagakusho, the Max Planck Society, and the Higher Education Funding Council for England. The SDSS Web Site

is <http://www.sdss.org/>.

This publication makes use of data products from the Wide-field Infrared Survey Explorer, which is a joint project of the University of California, Los Angeles, and the Jet Propulsion Laboratory/California Institute of Technology, funded by the National Aeronautics and Space Administration.

## REFERENCES

- Abazajian, K. N., Adelman-McCarthy, J. K., Agüeros, M. A., et al. 2009, *ApJS*, 182, 543.
- Benford, G. & Protheroe, R. 2008, *MNRAS*, 383, 663.
- Berrington, R. C., Lugger, P. M. & Cohn, H. N. 2002, *ApJ*, 123, 2261.
- Bourdin, H. & Mazzotta, P. 2008, *A&A*, 479, 307.
- Brentjens, M. A. 2008, *A&A*, 489, 69.
- Brentjens, M. A. & de Bruyn, A. G. 2005, *A&A*, 441, 1217.
- Bridle, A. H. & Fomalont, E. B. 1976, *A&A*, 52, 107.
- Bridle, A. H., Fomalont, E. B., Miley, G. K. & Valentijn, E. A. 1979, *A&A*, 80, 201.
- Briel, U. G., Henry, R. A., Schwarz, et al. 1991, *A&A*, 246, L10.
- Brunetti, G. & Jones, T. W. 2014, *International Journal of Modern Physics D*, 23, 1430007.
- Churazov, E., Brüggen, M., Kaiser, C. R., Böhringer, H. & Forman, W. 2001, *ApJ*, 554, 261.
- Clarke, T. E. & Ensslin, T. A. 2006, *AJ*, 131, 2900.
- de Gouveia dal Pino, E. M. & Lazarian, A. 2005, *A&A*, 441, 845.
- Dreyer, J. L. E. 1888, *MNRAS*, 49, 1.
- Drury, L. O'C 2012, *MNRAS*, 422, 2474.
- Fabian, A. C. & Daines, S. J. 1991, *MNRAS*, 252, 17p.
- Fabricant, D. L., Kent, S. M., & Kurtz, M. J. 1989, *ApJ*, 336, 77.
- Feretti, L., Giovannini, G., Govoni, F. & Murgia, M. 2012 *A&A Rev.*, 20, 54.
- Gieseler, U.D.J., Jones, T. W. & Kang, H. 2000, *A&A*, 364, 911.
- Greisen, E. W. 2014, *AIPS Cookbook*, (National Radio Astronomy Observatory).
- Govoni, F., Feretti, L., Giovannini, G., et al. 2001, *A&A*, 376, 803.
- Gunn, J. E. & Gott, J. R. 1972, *ApJ*, 176, 1.
- Hines, D. C., Owen, F. N., & Eilek, J. A. 1989, *ApJ*, 347, 713.
- Kale, R. & Dwarakanath, K. S. 2010, *ApJ*, 718, 939.
- Kang, H., Ryu, D. & Jones 2012, *ApJ*, 756, 97.
- Lal, D. V. & Rao, A. P. 2004, *A&A*, 420, 491.
- Miller, N. A., Owen, F. N. & Hill, J. M. 2003, *ApJ*, 125, 2393.
- Miller, N. A., Owen, F. N., Hill, J. M., Keel, W. C., Ledlow, M. J. & Oegerle, W. R. 2004, *AJ*, 129, 26.
- Mohr, J. J., Mathiesen, B. & Evrard, A. E. 1999, *ApJ*, 517, 627.
- Owen, F. N., Eilek, J. A. & Kassim, N. E. 2000, *ApJ*, 543, 611.
- Owen, F. N., Hardee, P. E. & Cornwell, T. J. 1989, *ApJ*, 340, 698.
- Owen, F. N. & Rudnick, L. 1976, *ApJ*, 205, L1.
- Pfrommer, C. & Jones, T. J. 2011, *ApJ*, 739, 22.
- Pinzke, A., Oh, S. P., & Pfrommer, C. 2013, *MNRAS*, 435, 1061.
- Priest, E. & Forbes, T. 2000, *Magnetic Reconnection* (Cambridge: Cambridge University Press)
- Rau, U & Cornwell, T. J. 2011, *A&A*, 532, A71.
- Ricker, P. M. & Sarazin, C. L. 2001, *ApJ*, 561, 621.
- Roediger, E. & Brüggen, M. 2006, *MNRAS*, 369, 567.
- Roettiger, K., Burns, J. O. & Pinkney, J. 1995, *ApJ*, 453, 634.
- Roettiger, K., Stone, J. M., & Mushotzky, *ApJ*, 493, 62.
- Romanova, M. M. & Lovelace, R. V. E. 1992, *A&A*, 262, 26.
- Röttgering, H., Snellen, I., Miley, et al. 1994, *ApJ*, 436, 654.
- Rudnick, L. & Owen, F. N. 1976 *ApJ*, 203, L107
- Schnitzeler, D. H. F. M., Katgert, R. & de Bruyn, A. G. 2009, *A&A*, 494, 611.
- Sijbring, D. & de Bruyn, A. G., 1998, *A&A*, 331, 901.
- Skillman, S. W., Xu, H., Hallman, E. J., et al. 2013, *ApJ*, 765, 21.
- Sun, M., Murray, S., Markevitch, M., & Vikhlinin, A. 2002, *ApJ*, 565, 867.
- Takizawa, M. 2000, *ApJ*, 532, 183.
- Tamura, T., Hayashida, K., Ueda, S. & Nagai, M. 2011, *PASJ*, 63, S1009.
- Tonry, J. 1985a *ApJ*, 291, 45.
- Tonry, J. 1985b, *AJ*, 90, 2431.
- van Weeren, R. J., Intema, H., Oonk, J. B. R., Röttgering, H. J. A., & Clarke, T. E. 2009, *A&A*, 508, 1269.
- van Weeren, R. J., Röttgering, H. J. A., Brüggen, M. & Hoeft, M. 2010, *Science*, 330, 347.
- van Weeren R. J., Röttgering, H. J. A., Intema, H. T., et al 2012b, *A&A*, 546, A124.
- van Weeren, R. J., Röttgering, H. J. A., Rafferty, D. A., et al. 2012a, *A&A*, 543, A43.
- Vijayaraghavan, R. & Ricker, P. M. 2013, *MNRAS*, 435, 2713.
- Wright, E. L., Eisenhardt, P. R. M., Mainzer, A. K., et al. 2010, *AJ*, 140, 1868.